Principal component analysis for fermionic critical points

Natanael C. Costa,[1,2,*] Wenjian Hu,[2,3] Z. J. Bai,[3] Richard T. Scalettar,[2] and Rajiv R. P. Singh[2]
[1]*Instituto de Fisica, Universidade Federal do Rio de Janeiro Cx.P. 68.528, 21941-972 Rio de Janeiro RJ, Brazil*
[2]*Department of Physics, University of California Davis, California 95616, USA*
[3]*Department of Computer Science, University of California Davis, California 95616, USA*
(Received 22 August 2017; published 20 November 2017)

We use determinant quantum Monte Carlo (DQMC), in combination with the principal component analysis (PCA) approach to unsupervised learning, to extract information about phase transitions in several of the most fundamental Hamiltonians describing strongly correlated materials. We first explore the zero-temperature antiferromagnet to singlet transition in the periodic Anderson model, the Mott insulating transition in the Hubbard model on a honeycomb lattice, and the magnetic transition in the 1/6-filled Lieb lattice. We then discuss the prospects for learning finite temperature superconducting transitions in the attractive Hubbard model, for which there is no sign problem. Finally, we investigate finite temperature charge density wave (CDW) transitions in the Holstein model, where the electrons are coupled to phonon degrees of freedom, and carry out a finite size scaling analysis to determine T_c. We examine the different behaviors associated with Hubbard-Stratonovich auxiliary field configurations on both the entire space-time lattice and on a single imaginary time slice, or other quantities, such as equal-time Green's and pair-pair correlation functions.

DOI: 10.1103/PhysRevB.96.195138

I. INTRODUCTION

Deep connections between neural networks, statistical physics, and biological modeling were established starting more than three decades ago. Hopfield, for example, proposed [1] a description of "neurons" whose stable limit points could be used to store specific "memories," and whose structure was basically that of an Ising model with symmetric, long-range interactions. A central result was the emergence of collective properties such as the ability to "generalize" to related memories. Concepts from spin glass theory and frustrated order were shown to have close analogues with neural networks, including limitations on the ability to store competing memories, the existence of critical temperatures for the stability of specific spin patterns (memories), with additional mixed patterns becoming stable at yet lower temperature, the role of asymmetric exchange constants (synaptic strength), and so forth [2–7].

Over the past several years, the use of neural networks and learning algorithms has been revisited with fresh perspectives and, in particular, with a focus on the possibility that appropriately defined networks might be useful in locating phase transitions. For instance, self-learning algorithms can strongly reduce the autocorrelation from the critical slowing down in second-order phase transitions [8–10]. Furthermore, it was shown [11] that PCA could provide a useful diagnostic of the phase transition in an Ising model in the zero-magnetization sector, where two ferromagnetic domains dominate the partition function at low temperature. An extention of this PCA analysis had been done to several other classical models, e.g., the Blume-Capel model, which have first-order transitions and tricritical points [12]. Recently, PCA also has been shown relevant for the investigation of the nature of frustrated classical spin models [13].

The well-known exact mapping between the 2D classical Ising model and the 1D quantum Ising model in a transverse magnetic field immediately implies that this ability to distinguish a finite temperature transition in the former case implies that the zero-temperature quantum critical point (QCP) can be determined in the latter. However, while it is true that all quantum models can be mapped to classical models in one higher dimension, in most cases, the equivalent classical is very complex, for example, for fermions typically depending on a determinant whose entries include the degrees of freedom in the simulation. It thus remains an open question whether a QCP can be located by learning methods, although certainly the allowed presence of long-range connections in networks suggests they might be promising.

There have been several recent attempts to combine machine learning techniques and DQMC. Ch'ng *et al.* [14] have shown that convolutional neural networks (CNN) can successfully *generalize* the Neél temperature T_N of the three-dimensional Hubbard model at half-filling. That is, a network trained at weak ($U/t = 5$) and strong ($U/t = 16$) coupling can predict T_N at intermediate U/t, and make inferences concerning the AF transition when the system is doped (a parameter regime for which the sign problem prevents direct DQMC simulations at low temperature). Meanwhile, Broecker *et al.* [15] have also used DQMC for the Hubbard model together with CNN with a focus on understanding if the sign problem can be circumvented. Learning about the sign problem is also implicit in machine learning studies of the nodal surfaces of many-electron wave functions [16]. A particularly intriguing proposal uses a machine-learned effective bosonic action to guide proposed moves at a much lower cost than the usual cube of the system size [17–19].

Neural networks have also been used in combination with QMC to provide information of quantum phase transitions [20–22], topological states [23–26], many-body localization [22,27], and entanglement properties [28]. Furthermore, neural networks are useful to fit functional forms for potential energy surfaces which are then used in subsequent simulations [29].

*natanael@if.ufrj.br

In contrast to the situations described above, where DQMC is applied to tight-binding Hamiltonians and the energy scales U, t, T, and μ are unambiguously known, in these studies the network is used to avoid complicated and somewhat arbitrary fits to the functional form of the potential energy, allowing for more robust molecular dynamics simulations.

Much of the work described above has utilized "supervised" learning approaches in which the nature of the phases is provided in certain parameter regimes with the goal of extrapolating the properties of the patterns to other regimes. Unsupervised methods have also been used to investigate properties of quantum systems [30,31]. Here, we study the ability of unsupervised learning methods to determine the location of the QCP in several models of interacting, itinerant electrons, when provided with data from DQMC simulations. Using PCA, we analyse five cases, including spin, charge and pair ordering. Concerning magnetic transitions, we investigate (i) the antiferromagnetic (AF)-singlet transition in the periodic Anderson model (PAM), a Hamiltonian which describes the coupling of a noninteracting ("metallic") fermionic species with a strongly correlated ("localized") one; (ii) the paramagnetic metal to insulating antiferromagnet QCP, which occurs at a nonzero U_c in the repulsive Hubbard model on a honeycomb lattice [32–36]; and (iii) the AF ground state for the Hubbard model on the "Lieb lattice" at electronic density $\rho = 1/3$, which is closely related to the AF phase in nondoped cuprates. We likewise study pair ordering in (iv) the attractive Hubbard model in the square lattice, which exhibits a finite temperature phase transition to a s-wave superconducting state. Finally, charge ordering is investigated in (v) the Holstein model, one of the simplest Hamiltonians to take into account electron-phonon coupling. Periodic boundary conditions have been used throughout this paper. Our methodology focusses on determining whether the signatures of the transitions occur through an examination of the principle components of matrices constructed from snapshots of the degrees of freedom during the course of a simulation.

This paper is organized as follows. The DQMC method and the PCA procedure are introduced in Sec. II. The PCA analysis of the PAM is presented in Sec. III, while the results for Hubbard model on honeycomb and the Lieb lattices are exhibited in Secs. IV and V, respectively. The attractive Hubbard and Holstein models are left to Secs. VI and VII. The sections are self-contained, with the individual models being briefly introduced in each.

II. METHODOLOGY

DQMC [37] is an approach for solving interacting fermion Hamiltonians exactly (to within statistical error bars) on lattices of finite size. The central observation of the method is that the partition function $\mathcal{Z}$ for two fermionic species $\sigma = \uparrow, \downarrow$ interacting with a space and imaginary time dependent bosonic field $\mathcal{S}(i,\tau)$, but *not* with each other, can be written as

$$\mathcal{Z} = \sum_{\{S(i\tau)\}} \prod_{\sigma} \det(I + B_\sigma(1)B_\sigma(2)B_\sigma(3)\cdots B_\sigma(L)). \quad (1)$$

Here the identity matrix I and the matrices $B_\sigma(\tau)$ have dimension the spatial lattice size N, and L is the number of imaginary time slices into which the inverse temperature β is divided. The sum is over configurations of the bosonic field. Each $B_\sigma(\tau)$ is the product of the exponential of the kinetic energy matrix K, which is usually independent of σ, and a diagonal matrix $V_\sigma(\tau)$ whose entries are $V_{ii\,\sigma}(\tau) = g_\sigma \lambda \mathcal{S}(i,\tau)$.[1] Here, λ is the coupling constant between the fermionic and bosonic variables and $g_\sigma = \pm 1$ depends on the model. For Hamiltonians with repulsive interactions, g_σ most commonly has opposite sign for the two spin species, while for Hamiltonians with attractive interactions, g_σ is the same for both σ. (It is possible to choose g_σ to have the same sign for repulsive interactions, at the expense of introducing an imaginary coupling constant λ.) The separation into exponentials of K and V necessitates an inverse temperature discretization $\Delta\tau = \beta/L$. This is taken small enough so that systematic "Trotter errors" are smaller than statistical error bars.

The Holstein Hamiltonian (see Sec. VI B) immediately satisfies the description above. The field $\mathcal{S}(i\tau)$ is comprised of the space-imaginary time values arising from a path integral expression for the quantum phonon variables. For the Hubbard model, $\mathcal{S}(i,\tau)$ are the space-time components of a Hubbard-Stratonovich (HS) field introduced to decouple the fermion-fermion interaction. In this paper, we employ the discrete version of the HS transformation introduced by Hirsch [38]. Hirsch has shown [38,39] that the correlation functions of the HS variables are directly related to spin-spin correlations of the fermionic degrees of freedom, suggesting that success with using magnetic configurations in PCA studies of classical transitions [11,12] might be replicated with HS configurations.

Principal component analysis [40–42] is an unsupervised learning technique in which, for the implementation here, configurations of the HS field configurations generated in the course of a set of DQMC simulations are assembled in the rows of a matrix F. The number of columns of F is the dimension of the HS field (either the spatial lattice size N or the full space-time lattice size, see below.) The number of rows of F is the number of configurations. Typically, we will input l configurations for each of t different simulations, which might correspond to different values of an energy scale in the Hamiltonian, the temperature, or the density. Thus the number of rows of F is $M = lt$. The mean values of each column of F are subtracted to produce a "data-centered" matrix X.

The most straightforward description of the PCA procedure is that the eigenproblem of the real symmetric matrix $X^T X$ is solved, yielding eigenvalues λ_n and eigenvectors w_n. The distribution of the "relative variances" $\tilde{\lambda}_n = \lambda_n / \sum_{i=1}^{N} \lambda_i$, and in particular the existence of a gap separating a few dominant $\tilde{\lambda}_n$ from the others, provides information about possible phase transitions. Following the work of Wang [11], we will plot the ordered pairs of the first two principle components, the inner products of the eigenvectors of $\mathbf{X}$ with the two largest eigenvalues, and the *individual* HS field configurations, and also study the quantified principle components, which are the

[1] This description of the matrix structure in DQMC is appropriate for the models studied in this paper. However, DQMC can also be used in situations (such as the Su-Schrieffer-Heeger model) in which the bosonic field modulates the fermion hopping. In such situations, K becomes τ dependent and the bosonic field enters its matrix elements.

averages of the principle components over the l configurations of a particular simulation.

The above presentation of PCA has the virtue of being brief, but does not provide a detailed look at what the PCA is actually extracting from the data. For a more complete exposition see Refs. [40–42].

There are several possible implementations of PCA within the context of DQMC. Here we will, for example, examine whether any differences arise between constructing the PCA matrix $\mathbf{X}$ from the bosonic field configuration $\mathcal{S}(i,\tau)$ allowing i to vary over all N spatial sites at a single *fixed* τ, as opposed to using $\mathcal{S}(i,\tau)$ for all i and also all $\tau = 1,2,\ldots,L$. We will also, as previously explored by Broecker *et al.* [15] for the repulsive Hubbard model, compare training of a network with the fermionic Greens function, $G = (I + B(1)B(2)\cdots B(L))^{-1}$, rather than the HS field configuration.

III. RESULTS: AF-SINGLET TRANSITION IN THE PAM

We first consider the AF-singlet transition, commonly observed in heavy-fermion materials [43], in which two species of electrons, conduction (d) and localized (f) electrons, experience a hybridization V, which can be tuned by adjusting external parameters, such as pressure. At low V, the Ruderman-Kittel-Kasuya-Yosida (RKKY) interaction leads to long-range magnetic order (LRO), while for large V local singlets form, usurping LRO. A quantum phase transition (QPT) occurs for a critical hybridization V_c separating these distinct ground states. The signature of this QCP is observed even at finite temperature, with the appearance of non-Fermi liquid behavior.

The standard models for heavy-fermion materials are the Kondo lattice model (KLM) [44–48] and the periodic Anderson model (PAM) [49–52]. We consider the latter, for which the Hamiltonian is

$$H = -t\sum_{\langle \mathbf{i},\mathbf{j}\rangle\sigma}(d^\dagger_{\mathbf{i}\sigma}d_{\mathbf{j}\sigma} + \text{H.c.}) - V\sum_{\mathbf{i}\sigma}(d^\dagger_{\mathbf{i}\sigma}f_{\mathbf{i}\sigma} + \text{H.c.}) + U\sum_{\mathbf{i}}\left(n^f_{\mathbf{i}\uparrow} - \frac{1}{2}\right)\left(n^f_{\mathbf{i}\downarrow} - \frac{1}{2}\right). \quad (2)$$

Here, $\mathbf{i}$ runs over sites in a two-dimensional square lattice, with $\langle \mathbf{i},\mathbf{j}\rangle$ denoting nearest neighbors. t is the hopping integral of conduction d electrons, and U the on-site Coulomb repulsion in the f band, while their hybridization is V. The fermion creation (annihilation) operators of conduction and localized electrons with spin σ on a given site $\mathbf{i}$ are $d^\dagger_{\mathbf{i}\sigma}(d_{\mathbf{i}\sigma})$ and $f^\dagger_{\mathbf{i}\sigma}(f_{\mathbf{i}\sigma})$, respectively. As written, the PAM in Eq. (2) has particle-hole symmetry (PHS) so that the density of each electron species obeys $\langle \rho^d_{\mathbf{i}\sigma}\rangle = \langle \rho^f_{\mathbf{i}\sigma}\rangle = 1/2$ at all t, U, V, and temperatures. At this half-filling, the AF-singlet QCP occurs at $V_c \approx 0.99\,t$ for $U = 4\,t$ [52]. Hereafter we set $t = 1$ as the scale of energy.

Providing the PCA procedure with the full space-time HS fields for a simulation on an 12×12 lattice at $U = 4$ and $\beta = 24$ (i.e., $L = 192$ and $\Delta\tau = 1/8$) for different values of V, we obtain the results exhibited in Fig. 1. For each hybridization we provided $l = 1000$ independent configurations. The relative variance $\tilde{\lambda}_n$ for different components n are displayed in Fig. 1(a), in which the first component is dominant. It has been suggested [12] that the appearance of sharp falloff from

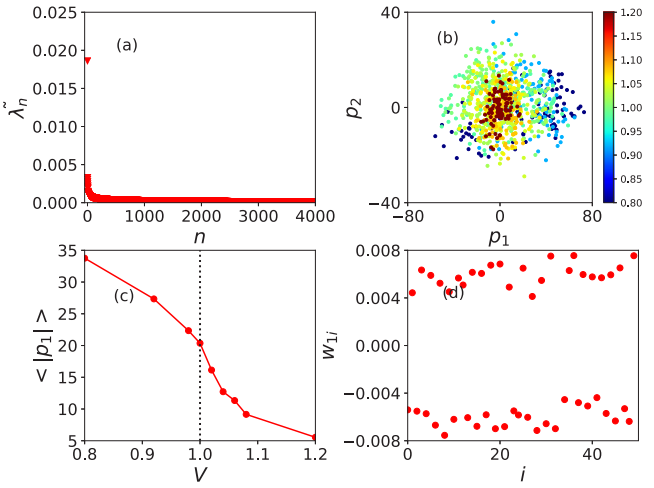

FIG. 1. PCA results for the PAM, with lattice size $N = 12\times12$, inverse temperature $\beta/t = 24$ and on-site repulsion $U = 4$. (a) Relative variances $\tilde{\lambda}_n$ obtained from the raw HS field configurations, with the horizontal axis indicating corresponding component labels. (b) Projection of the raw HS field configurations onto the plane of the two leading principal components. Data points are color-coded by the value of the hybridization V (bar at far right). For large V (i.e., in the singlet phase), the pairs form a single small structure centered at (0,0). For small V (i.e., in the AF phase), the pairs spread out around the origin. (c) The quantified first leading component as a function of V. The dashed line, corresponding to the steepest transition, indicates the QCP at $V_c \approx 1.0$. (d) The weight vector corresponding to the first leading component, which shows a clear AF pattern.

dominant relative variances (e.g., $\tilde{\lambda}_1$) is indicative of a single dominant spin pattern, e.g., AF order. Figure 1(b) presents the projection of the two leading principal components, with the data points of large hybridization localized around the origin. For low hybridization, the collection of points bifurcates, i.e., it appears as two separate clusters indicating the presence of two separate broken symmetry ground states. This change is similar to what is seen in finite temperature transitions in classical spin models. Here, we interpret the analogous behavior as signaling a QPT at a critical V_c.

The position of the QCP can be roughly inferred via the behavior of the quantified first leading component as a function of V, as displayed in Fig. 1(c). For low hybridizations, $\langle |p_1| \rangle$ is large, while it is suppressed at large hybridizations, behaving similar to the AF structure factor. One can estimate the QCP location at the inflection point, $V_c \approx 1$, where the $\langle |p_1| \rangle$ is most rapidly changing. This V_c is in agreement with conventional approaches based on finite size scaling of the AF structure factor [49,52], $V_c \sim 0.99\,t$, although at present the PCA analysis is clearly considerably less accurate. That order at wave vector $\mathbf{q} = (\pi,\pi)$ is demonstrated by the structure of the first eigenvector, Fig. 1(d), which has an obvious alternation in sign for sites on the two sublattices. In classical transitions [12], the quantified leading components mimic physical quantities such as magnetization and susceptibility. Interestingly, the quantified first leading component of the PAM also resembles the mean-field magnetization, as shown in Fig. 2 of the Ref. [52].

Notably, it has been suggested [12] for classical models that the number of distinct groupings of the (p_1, p_2) distributions reflects the degeneracy of the ground state: two groups in the Ising case where spins can order either up or down, a continuous ring around the origin for the XY model, and four peaks for a biquadratic Ising model, which possesses four ordered phases. The AF order in the PAM, and in the Hubbard and Lieb models below, has a continuous symmetry similar to the XY case. However, the HS transformation used here, and in many DQMC simulations, couples preferentially to the z component of the fermion spin. This choice does *not* represent any approximation in the results for physical observables obtained by DQMC, but is known to break symmetries in quantities like *error bars*, which are algorithm-dependent. The (p_1, p_2) distributions, shown in Fig. 1(b), are more symmetrically distributed about (0,0) than for the Ising model [11], because the system size is still relative small and the temperature is low but not zero.

If a rotationally invariant HS decoupling is performed, and the resulting configurations are fed into the PCA, symmetry is preserved and similar results to the XY model are expected. There are very significant drawbacks to this approach. The two spin species are mixed by coupling of an HS field S_x to the x component of the fermion spin, i.e., $S_x\,(c^\dagger_{i\uparrow}c_{i\downarrow} + c^\dagger_{i\downarrow}c_{i\uparrow})$. As a consequence, the two independent spin-up and spin-down Greens functions (and fermion determinants) become a single matrix with double the dimension. This fundamental change in the algorithm, which several groups have attempted, including ourselves [53,54], is known (in the case of the Hubbard model) to worsen the sign problem. In the present case of the Holstein model, there is no sign problem precisely because there are two separate determinants whose square is always positive. In addition, the execution time is significantly increased by the necessity of inversion of a larger matrix.

IV. RESULTS: AF-PM TRANSITION ON A HONEYCOMB LATTICE

We next investigate the Hubbard Hamiltonian,

$$H = -t \sum_{\langle \mathbf{i},\mathbf{j}\rangle\sigma} (d^\dagger_{\mathbf{i}\sigma} d_{\mathbf{j}\sigma} + d^\dagger_{\mathbf{j}\sigma} d_{\mathbf{i}\sigma}) + U \sum_{\mathbf{i}} \left(n^d_{\mathbf{i}\uparrow} - \frac{1}{2}\right)\left(n^d_{\mathbf{i}\downarrow} - \frac{1}{2}\right), \quad (3)$$

on a honeycomb lattice. Unlike the square lattice, in this geometry, a critical value U_c is required in order to obtain an AF ground state at half-filling [32–36]. A metal-insulator transition also occurs at U_c, in contrast with the PAM, where both AF and singlet phases are insulators.

Here, we examine the use of the PCA to discern the finite U_c required to induce AF order. We performed simulations on a 12×12 lattice at $\beta = 20$ (i.e., $L = 160$ and $\Delta\tau = 1/8$), and providing $l = 1000$ independent configurations for each value of U. In Fig. 2(a), we observe, as for the PAM, a single dominant relative variance. The pairs of the two largest components are shown in Fig. 2(b), and provide information about the QCP: a group of points centered around the origin for small U spreads out rapidly for large U. An estimation of the QCP is obtained from the quantified first leading component as a function of U, exhibited in Fig. 2(c). For a better determination of the inflection point one can perform a numerical fitting of the DQMC data, with its differentiation providing a maximal value for $d\langle|\,p_1\,|\rangle/dU$ at $U \approx 4.4$, as displayed in the inset of Fig. 2(c). This result is reasonably close to the critical value obtained by conventional methods, where $U_c \approx 3.85$ [36]. However, the evolution of $\langle|p_1|\rangle$ is quite gradual. The estimation of U_c will likely be improved with the analysis of different lattice sizes [12]; e.g., see Sec. VII. It appears the determination of the QCP is less accurate using the PCA than from conventional scaling methods on lattices of the same size, as was also seen in the preceding section for the PAM. Examination of the eigenvector [Fig. 2(d)] reveals a staggered pattern which indicates the ordering is AF.

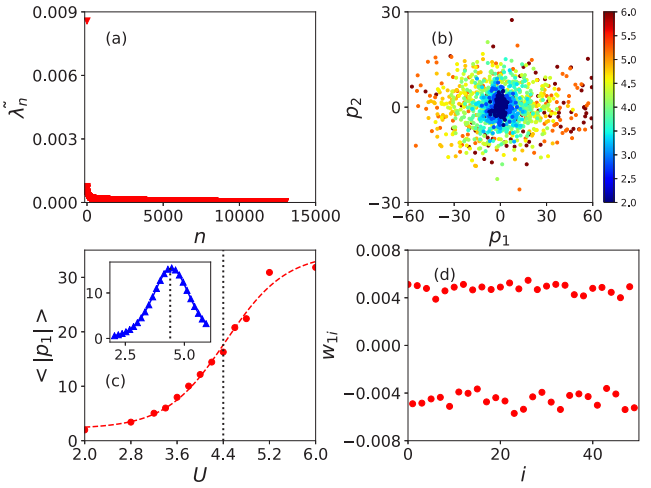

FIG. 2. PCA results for the honeycomb lattice (single band) Hubbard model, with the lattice size $N = 12\times12$, the inverse temperature $\beta/t = 20$. (a) Relative variances $\tilde{\lambda}_n$ obtained from the raw HS field configurations. (b) Projection of the raw HS field configurations onto the plane of the two leading principal components. Data points are color-coded by the value of the onsite repulsion U (bar at far right). For small U (i.e., in the paramagnetic phase), the pairs are localized near (0,0). For larger U (i.e., in the AF phase), the pairs spread out around the origin. (c) The symbols correspond to the quantified first leading component as a function of U, while the dashed (red) curve is just a guide to the eye. The vertical (black) dotted line, corresponding to the steepest transition, indicates the QCP at $U_c \approx 4.4$. The inset displays the numerical derivative. (d) The weight vector that corresponds to the first leading component, which shows a clear AF pattern.

V. RESULTS: LIEB LATTICE AT 1/6 FILLING

As a final illustration of magnetic transitions in the ground state, we study the repulsive Hubbard Hamiltonian on the "Lieb lattice." In contrast to the two previous cases, where energy scales V and U are used to tune through the QCP, the transition is explored as a function of filling. The Lieb lattice describes a three-band model formed by an underlying square lattice which is then decorated with additional sites on each bond. The Lieb lattice is bipartite, but has a different number of sites on the two sublattices. An interesting feature of this geometry is the presence, in the noninteracting limit, of a perfectly flat energy band, sandwiched between two dispersing

bands, which can lead to ferromagnetism when U is turned on at half-filling [55].

In a seminal paper, Lieb showed that the Hubbard model on this lattice at half-filling exhibits long-range ferrimagnetic order in its ground state [56]. The spin order in similar geometries has been explored in Refs. [57–61]. In addition to these rigorous results, the Lieb lattice is of interest as a more faithful representation of the CuO_2 sheets of cuprate superconductors than is provided by the single band Hubbard model. In this three band case, the repulsion U is typically chosen to take different values on the square lattice and bridging sites. The implications of inhomogeneous U for ferrimagnetism were recently explored in Ref. [62].

Lieb's theorem is of limited direct interest for cuprate superconductivity since it describes a filling of the lattice $n = 3$ holes per CuO_2 unit cell, far from that actually present in these materials, $n = 1 + \delta$. Although there are no rigorous theorems available for the nature of the spin order away from half-filling, previous results provide evidence of antiferromagnetic correlations for one hole per unit cell, which are strongly suppressed for small doping δ [63–65]. The investigation of other phases, such as superconductivity for small doping, remains a challenge.

Here we apply PCA to determine the enhancement of antiferromagnetic correlations for Hubbard model in the Lieb lattice at fillings around one hole per unit cell (or $\rho = 1/3$). Away from half-filling, the measurements of physical quantities by DQMC are strongly impeded by the sign problem, see, e.g., Ref. [66]. Since the PCA procedure can be provided with HS fields without the necessity of dividing by the average sign, it can be undertaken even when the average sign is small. It should be noted, however, that even in this case the HS fields are generated with the absolute value of the determinants, and it remains an open question how much this will bias the physics [67]. We return to this point in the conclusions.

The Hubbard Hamiltonian on the Lieb lattice is

$$\begin{aligned} H = & -t_{pd} \sum_{\mathbf{r}\sigma} \left(d^{\dagger}_{\mathbf{r}\sigma}\, p^{x}_{\mathbf{r}\sigma} + d^{\dagger}_{\mathbf{r}\sigma}\, p^{y}_{\mathbf{r}\sigma} + \text{H.c.} \right) \\ & - t_{pd} \sum_{\mathbf{r}\sigma} \left(d^{\dagger}_{\mathbf{r}\sigma}\, p^{x}_{\mathbf{r}-\hat{x}\,\sigma} + d^{\dagger}_{\mathbf{r}\sigma}\, p^{y}_{\mathbf{r}-\hat{y}\,\sigma} + \text{H.c.} \right) \\ & + \sum_{\mathbf{r}\alpha} U_{\alpha} \left(n^{\alpha}_{\mathbf{r}\uparrow} - \frac{1}{2} \right) \left(n^{\alpha}_{\mathbf{r}\downarrow} - \frac{1}{2} \right) \\ & - \mu \sum_{\mathbf{r}\alpha\sigma} n^{\alpha}_{\mathbf{r}\sigma} \end{aligned} \tag{4}$$

with t_{pd} being hopping between d and p^{α} ($\alpha = x$ or y) orbitals. As before we define t_{pd} as unity. We investigate the inhomogeneous on-site repulsion case, with $U_p = 0$ and $U_d = 4$. For this choice of U_{α}, the particle-hole symmetric form of the interaction energy in Eq. (4) leads to a difference of on-site energies $\Delta\varepsilon_{dp} = 2$, which is close to the difference of on-site energies of oxygen and copper orbitals in the cuprates.

We performed simulations on a 10×10 lattice (i.e., 300 sites) at $\beta = 20$ (fixing $L = 160$ and $\Delta\tau = 1/8$), and providing $l = 1000$ independent configurations for each value of ρ. The relative variances $\tilde{\lambda}_n$ for different components n are displayed in Fig. 3(a). Although the subdominant values are more prominent than in the PAM and Hubbard model cases, λ_1 is still more than twice λ_2. The projection of the two largest

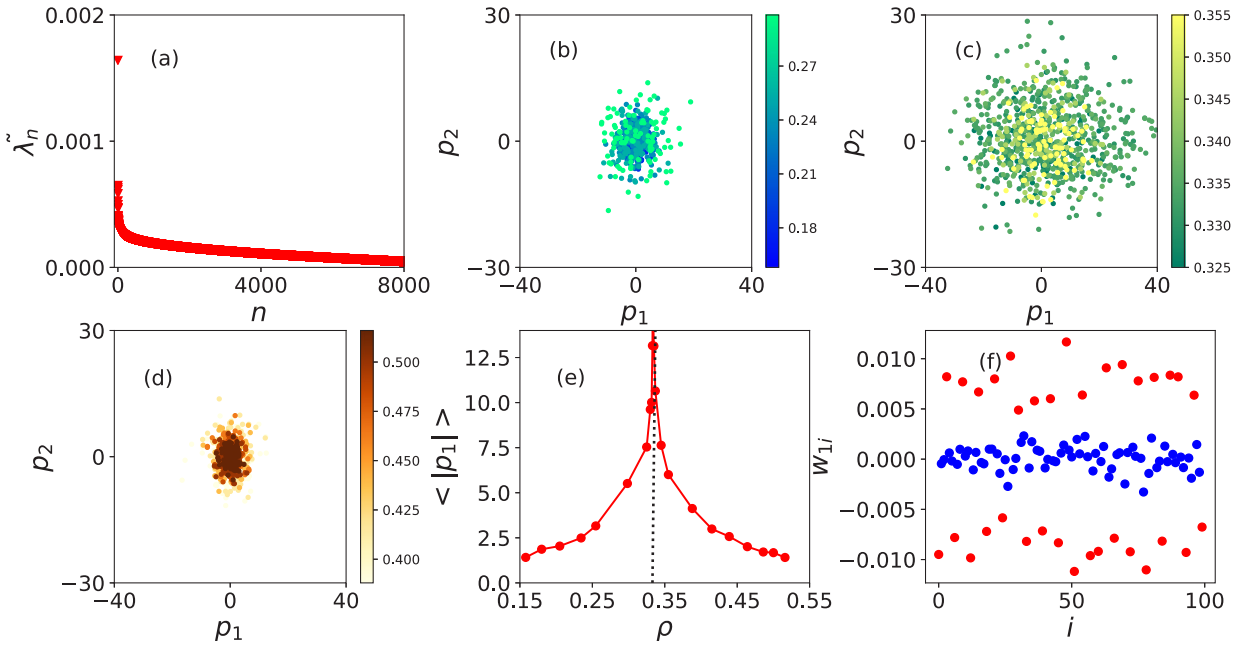

FIG. 3. PCA results for the Lieb lattice Hubbard model, with lattice size $N = 10\times10$, and inverse temperature $\beta/t = 20$. (a) Relative variances $\tilde{\lambda}_n$ obtained from the raw HS field configurations. (b)–(d) Projection of the raw HS field configurations onto the plane of the two leading principal components. Data points are color-coded by the value of the onsite density ρ (bar at far right). (e) The quantified first leading component as a function of ρ. The dashed line, showing the abrupt peak, indicates the QCP at $\rho_c \approx 1/3$, (f) The weight vector corresponding to the first leading component. Red dots represent (copper) d sites, while blue dots correspond to (oxygen) p sites.

components, is presented in Figs. 3(b)–3(d), for (b) $\rho < 1/3$, (c) $\rho \sim 1/3$, and (d) $\rho > 1/3$. Notice that for $\rho < 1/3$ and $\rho > 1/3$ the data points form a small cluster around the origin, whereas for $\rho \sim 1/3$ they are spread out, suggesting a disorder-order-disorder transition when ρ varies. Figure 3(e) exhibits the quantified first leading component as a function of ρ, with a sharp increase in $\langle|p_1|\rangle$ occuring at $\rho = 1/3$. A direct comparison can be made between the $\langle|p_1|\rangle$ and the AF structure factor of d sites, which provides evidence of an AF ground state at $\rho = 1/3$, in line with the conventional analysis [63–65]. Figure 3(f), the leading eigenvector, emphasizes that the magnetic order is on the "copper" sites of the square sublattice, while the "oxygen" bridging sites have nearly zero components.

VI. RESULTS: SUPERCONDUCTIVITY IN ATTRACTIVE HUBBARD MODEL

The previous sections have described the ability of PCA to learn about "quantum critical points" as energy scales in the Hamiltonian or density are varied. We now turn our attention to examining the finite temperature transition in the attractive Hubbard model.

At half-filling, and on a bipartite lattice, a particle-hole transformation (PHT) on the Hubbard Hamiltonian maps the attractive to the repulsive cases, so that the existence of AF order at $T = 0$ in the latter implies the presence of simultaneous CDW (the analog of AF in the z direction) and superconductivity (SC) order (the analog of AF order in the xy plane) in the former [68]. Thus the results of Sec. IV for the AF transition of the repulsive Hubbard model immediately imply that PCA can capture the SC-CDW transition in the ground state of the half-filled attractive Hubbard model on a honeycomb lattice. Away from half-filling it is known from the PHT, which maps the model to the repulsive model in an external Zeeman field, that there is a finite temperature Kosterlitz-Thouless (KT) transition [68] to a purely SC state. For instance, at $\rho = 0.80$ on a square lattice one obtains $T_c \approx 0.13$, as reported by Ref. [69].

Earlier work on the classical XY model [12] suggests PCA can capture aspects of KT physics—the presence of a transition—but not its physical origin in terms of vortex unbinding. We now use the method to investigate KT physics in a quantum Hamiltonian. The analysis of finite temperature transitions in the PCA approach is complicated by the fact that varying T changes the number of imaginary time slices at fixed $\Delta\tau$, and, therefore, the number of HS fields. Thus the number of columns of $\mathbf{X}$ varies over the t simulations. There are two possible solutions. One is to sweep the temperature by varying $\Delta\tau$ at fixed L. (If this is done, one must ensure $\Delta\tau$ remains small enough throughout is variation so that Trotter errors are minor.) The other approach is to give PCA only the HS variables on a single time slice. One might expect the PCA to be able to discern transitions even when not given the imaginary time evolution, since one knows that conventional approaches can analyze magnetic order both by using only equal-time measurements (the structure factor) or by analyzing unequal-time measurements (the susceptibility).

Figure 4 shows the results from both approaches, in which we fixed $U = -4$ in Eq. (3), and adjusted μ to have $\rho = 0.80$. In (a) and (b), the full space-time HS variables of a 12×12 square lattice are given to the PCA. The inverse temperature β is changed by altering $\Delta\tau = [0.03, 0.12]$ at fixed $L = 100$. We provided $l = 1000$ independent configurations for each

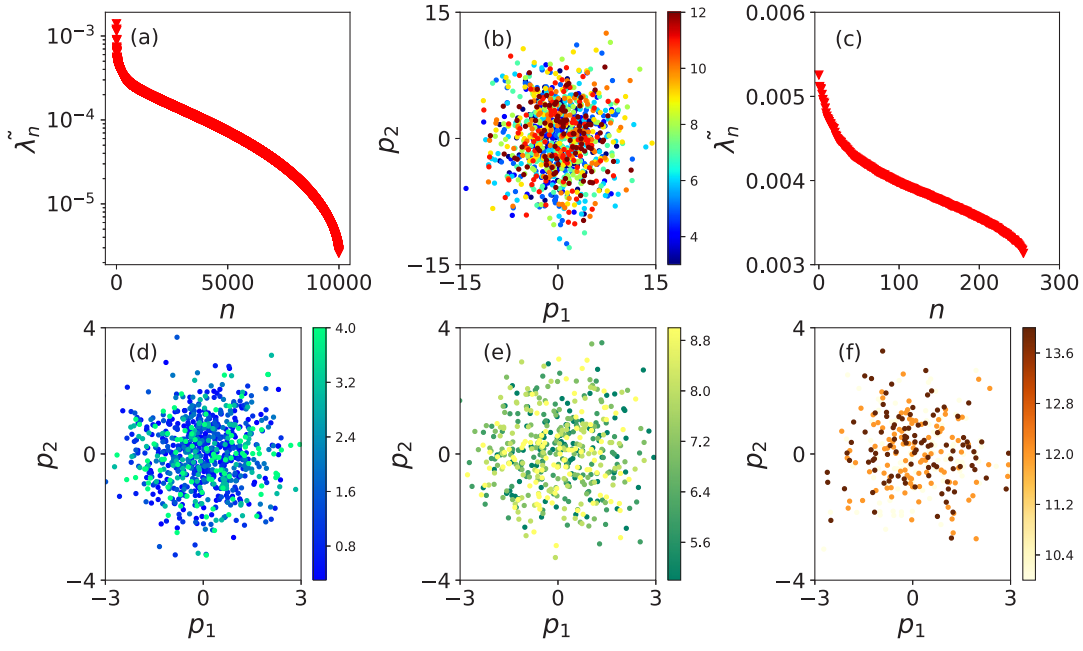

FIG. 4. Results of PCA analysis of the attractive Hubbard model. In (a) and (b), the full space-time HS field variables were used and β was altered over the range given by the color bar to the right of (b) at fixed L by varying $\Delta\tau$. The spatial lattice size was 12×12. In (c)–(f), the spatial lattice size was 16×16 and only the HS variables on a single slice were given to the PCA. In the latter case, for clarity, the (p_1, p_2) distribution is further separated into three panels.

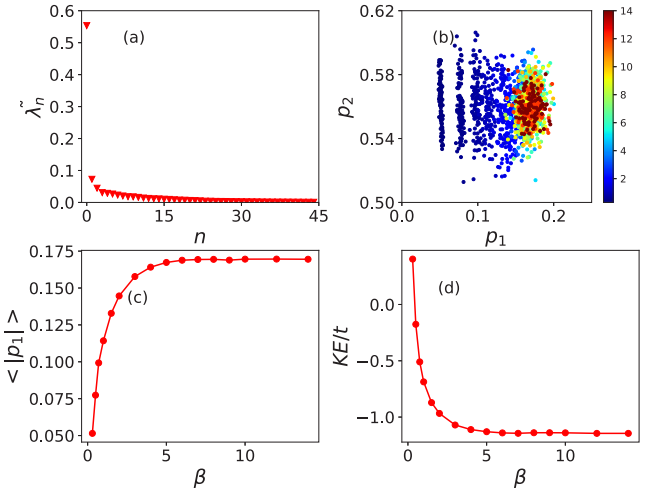

FIG. 5. PCA results for the attractive Hubbard model with lattice size $N = 16\times16$, on-site repulsion $U = -4$ and density $\rho = 0.8$. (a) Relative variances $\tilde{\lambda}_n$ obtained from the raw Green functions. (b) Projection of the raw Green functions onto the plane of the two leading principal components. The color bar indicates the inverse temperature β in units of t. (c) The quantified first leading component as a function of β. (d) The kinetic energy (KE) as a function of β.

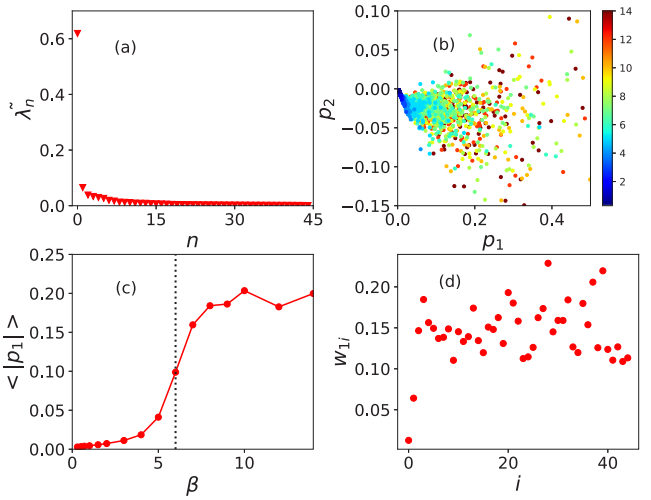

FIG. 6. PCA results for the attractive Hubbard model with the lattice size $N = 16\times16$, the on-site repulsion $U = 4$ and the density $\rho = 0.8$. (a) Relative variances $\tilde{\lambda}_n$ obtained from the raw pair pair correlation function. (b) Projection onto the plane of the two leading principal components. The color bar indicates the inverse temperature β in units of t. (c) The quantified first leading component as a function of β. The dashed line, corresponding to the steepest transition, indicates the QCP at $\beta_c \approx 6.0$. (d) The weight vector corresponding to the first leading component.

temperature to our PCA procedure. Panels (c)–(f) are concerning to single time slice measurements in a 16×16 square lattice at fixed $\Delta\tau = 0.125$ and varying L. For this latter case we provided $l = 4000$ independent measurements to PCA.

The PCA does not appear to capture the finite T SC transition in the attractive Hubbard model: there appears to be very little change in the geometry of the (p_1, p_2) distribution in going through T_c. This absence of a signal is true both when the full space-time field is provided [Fig. 4(b)] and also when just the spatial components are given [Figs. 4(d)–4(f)]. We also do not observe any relevant variation in the quantified first leading component as a function of β. A possible origin of this failure is that the HS field couples to the spin order, so that while it can, as seen earlier, carry information to the PCA about magnetic transitions, it is not able to do so for pairing transitions. In principle, it is possible to use HS fields, which couple to the pair creation and destruction operators, but this transformation results in a very bad sign problem, even for the attractive model [53].

Having seen inconclusive results when providing the PCA with the HS field configurations, we follow recent work [15] and employ the equal-time Green's functions, $G_{\mathbf{ij}}$. In contrast to Fig. 4(a), the relative variances now exhibit a single dominant component, as seen in Fig. 5(a). Furthermore, Fig. 5(b), data for the two largest components distinguish high and low temperatures. The quantified first leading component increases in magnitude as β increases [Fig. 5(c)], showing a very similar behavior to the kinetic energy (KE) of the system, exhibited in Fig. 5(d). This connection is not surprising. $G_{\mathbf{ij}}$ is closely related to the mobility of the electrons in the system, enabling the PCA to discern different regimes. However, the method does not capture the SC phase transition in the attractive Hubbard model, in the sense of showing a definitive signal near $\beta_c = 1/T_c \sim 7$. A similar smooth evolution of the kinetic energy ("effective hopping") is seen in the half-filled repulsive Hubbard model as U is increased [67].

As a final attempt to use the PCA to observe the SC transition in the attractive Hubbard model, we use the equal-time pair-pair correlation functions,

$$\Gamma_{\mathbf{ij}} = \langle d^\dagger_{\mathbf{i}\uparrow} d^\dagger_{\mathbf{i}\downarrow} d_{\mathbf{j}\downarrow} d_{\mathbf{j}\uparrow} + \text{H.c.} \rangle. \tag{5}$$

Figure 6(a) displays the relative variances of the principal components, whereas Fig. 6(b) exhibits the projection of the two largest components. The former presents a single dominant component, while the later shows two different behaviors to low and high temperatures. As before, we analyze the quantified first leading component $\langle |p_1| \rangle$ as a function of β. This is seen to behave in a similar way as the uniform Fourier transformation of the pair-pair correlation functions, P_s, as displayed in Fig. 6(c). These allow the PCA to provide the most promising signal of the SC phase transition around $\beta_c = 6$, in rough agreement with the known critical temperature $\beta_c \approx 7.5$ [69]. The conventional approaches which yield this value involve a demanding process of data collapses of P_s, a level of analysis which this initial PCA study here cannot attempt, since data on only a single lattice size are studied.

Unlike previous models where the ordering vector is (π,π), the pairing amplitude is uniform in the attractive Hubbard model. This is reflected in the lack of oscillations in the principal eigenvector, Fig. 6(d).

VII. RESULTS: CHARGE-DENSITY WAVE IN HOLSTEIN MODEL

Finally, we study the finite temperature CDW transition in the Holstein model [70], one of the simplest tight-binding models of the electron-phonon interaction (EPI). The Holstein model describes independent (i.e., dispersionless) quantum harmonic oscillators (HO) interacting locally with the electron density,

$$\mathcal{H} = -t \sum_{\langle \mathbf{i},\mathbf{j}\rangle,\sigma} (d^{\dagger}_{\mathbf{i}\sigma} d_{\mathbf{j}\sigma} + \text{H.c.}) - \mu \sum_{\mathbf{i},\sigma} n_{\mathbf{i},\sigma} - \lambda \sum_{\mathbf{i},\sigma} n_{\mathbf{i},\sigma} \hat{X}_{\mathbf{i}} + \frac{1}{2} \sum_{\mathbf{i}} \hat{P}^2_{\mathbf{i}} + \frac{\omega_0^2}{2} \sum_{\mathbf{i}} \hat{X}^2_{\mathbf{i}}. \quad (6)$$

As earlier, the sum over $\langle \mathbf{ij} \rangle$ is over nearest-neighbor sites on a two-dimensional square lattice. $\hat{P}$ and $\hat{X}$ are, respectively, the momentum and displacement operators of HOs with frequency ω_0 and mass $m = 1$. The electron-phonon coupling is λ, which, when integrated out, neglecting the $\hat{P}^2$ terms, leads to a dimensionless coupling, $\lambda_D = \lambda^2 / 2t\omega_0^2$.

The Holstein Hamiltonian is quadratic in the fermion operators, which can therefore be integrated out without the introduction of a HS field. The partition function then involves an integration over the phonon degrees of freedom,

$$Z = \int d\{x_{i,l}\} e^{-\Delta\tau S_B} [\det(I + B_1 B_2 \cdots B_L)]^2, \quad (7)$$

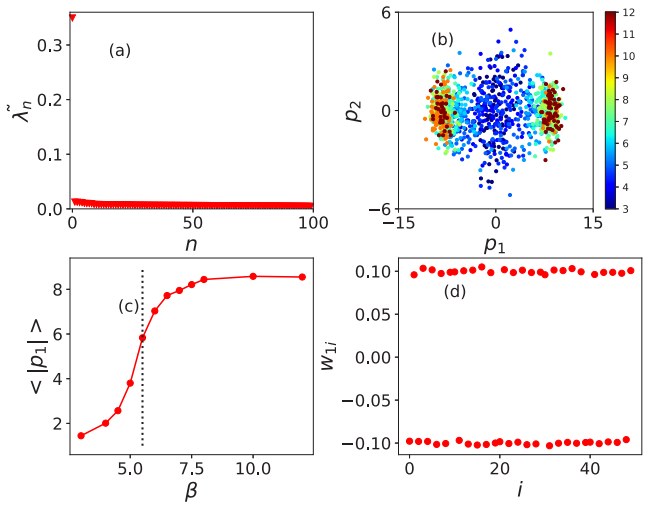

FIG. 7. PCA results for the half-filled 10×10 Holstein model for $\lambda_D = \omega_0 = 1$. (a) Relative variances $\tilde{\lambda}_n$ obtained from the raw phonon field configurations. There is a single dominant relative variance. (b) Projection of the raw phonon field configurations onto the plane of the two leading principal components. The color bar indicates the inverse temperature β in units of t. For small β (high T), the pairs evolve with the usual topologies: from a single grouping centered at (0,0) at small β (high T) to a pair of groupings at larger β (low T). (c) The quantified first leading component as a function of β. The dashed line indicates the QCP (separating the two topologies) $\beta_c \approx 5.5$ which is close to values obtained by conventional approaches. (d) The weight vector corresponding to the first leading component, which shows a clear (π,π) pattern.

with $\int d\{x_{i,l}\}$ being the integral over the set of continuous variables $x_{i,l}$ and

$$S_B = \sum_{i=1}^{N} \sum_{l=1}^{L} \left[\frac{1}{2m} \left(\frac{x_{i,l} - x_{i,l+1}}{\Delta\tau} \right)^2 + \frac{m\omega_0^2}{2} x_{i,l}^2 \right] \quad (8)$$

the phonon action. Because the phonons couple to the charge symmetrically for the spin-up and spin-down species, g_σ is the same for $\sigma = \uparrow, \downarrow$ and the two determinants are identical. Their product is always positive and there is no sign problem for any filling (as is also the case for the attractive Hubbard model). The phonon fields $\{x_{i,l}\}$ are sampled by standard Monte Carlo.

We used PCA to analyze the Holstein model at half-filling on a 10×10 square lattice. The PCA matrix was constructed from the phonon fields $\{x_{i,\tau}\}$, for a single fixed imaginary time slice τ, providing $l = 1000$ independent configurations for each temperature. Figure 7(a) displays the relative variances, which exhibit a single dominant component, suggesting the existence of a dominant phonon displacement (or a charge) pattern. The projection of the first two principal components [Fig. 7(b)] has data points (blue symbols) centered at the origin and high T, and split into two different clusters (red symbols) at low T. This splitting provides evidence of a phase transition for a critical T_c.

In addition to the changes in the scatter plots of Fig. 7(b) with temperature, we also analyze the quantified first leading component. Figure 7(c) displays the behavior of $\langle |p_1| \rangle$ as a function of β. A sharp increase is evident for inverse temperature in the range $4.5 \lesssim \beta \lesssim 6.5$. Taking the midpoint of this range suggests a PCA estimation for the critical temperature is $\beta_c \approx 5.5$. Although previous DQMC results provide evidence of $\beta_c = 8$ (see Refs. [71,72], respectively), a recent,

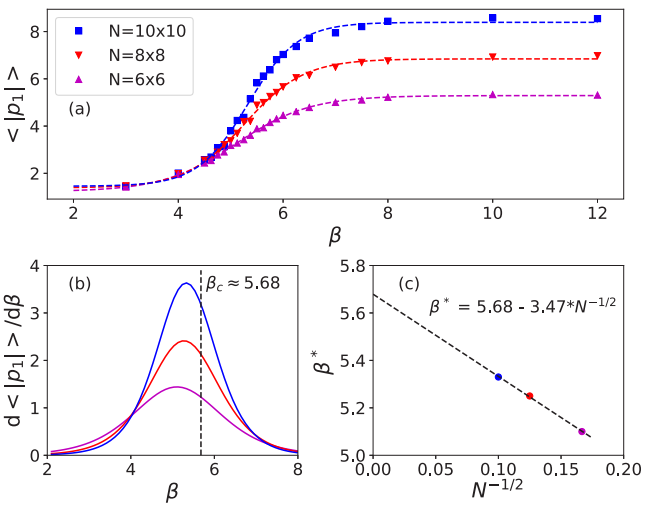

FIG. 8. Finite size scaling analysis of the Holstein model for $\lambda_D = \omega_0 = 1$. (a) Symbols are raw data for the quantified first leading component as a function of β, for different lattice sizes. The dashed lines are guides to the eye. (b) Derivatives with respect to β of numerical fits to the raw data. The dashed line marks the extrapolated critical value $\beta_c \approx 5.68$ obtained in (c) from a linear least-squares fit to the peaks β^* on different lattice sizes. We assume the finite size correction goes as the inverse of the linear system size.

more accurate, analysis determined $\beta_c = 6.0$ (Ref. [73]), in agreement with our PCA results.

To explore finite size effects, we compare simulations on lattice sizes $N = 6\times6$, 8×8, and 10×10. In Fig. 8(a), the symbols are the PCA/DQMC results for the quantified first leading component as a function of β, while the dashed lines are their corresponding numerical fits. Here we determine the inflection points by differentiating the fitted curves, following Sec. IV. Figure 8(b) displays the derivative of fitted curves, with the inflection points (and ultimately, the "critical temperatures") being determined by their peaks. In Fig. 8(c), we extract the critical value $\beta_c \approx 5.68$ using a linear least-squares fit on these inflection points. We have verified that fitting the data of Fig. 8(a) to different functional forms does not affect the values of β^*.

VIII. CONCLUSIONS

This paper has extended prior work [12] in which an unsupervised learning approach based on the PCA was applied to a variety of *classical* models of magnetism, to itinerant quantum Hamiltonians in two dimensions. The magnetic phase transitions in the Hubbard model on a honeycomb lattice, the periodic Anderson model, and the one sixth filled Lieb lattice, can all be observed via the evolution of the principal components, even though the transitions are tuned in quite different ways—via interaction strength, hybridization, and density, respectively.

The similarities extend to the finite temperature Kosterlitz-Thouless transition in the 2D attractive Hubbard Hamiltonian, which, like its classical XY counterpart, proves less amenable to analysis. In contrast, the finite temperature CDW transition in the half-filled 2D Holstein is well captured by the PCA, presumably because the broken symmetry is discrete.

The similarities between PCA for classical and quantum models of magnetism may be somewhat surprising, since, unlike short-range spin models, the effective classical degrees of freedom in DQMC are coupled by complicated, long-range interactions (the fermion determinants). Thus, in some ways, the application of PCA to configurations provided by DQMC reported here, and in Refs. [14,15], are similar to some of the original themes explored in the interplay of learning and statistical mechanics which considered (possibly frustrated) long-range models.

To see the full rotational symmetry of the magnetically ordered ground states of the Hubbard model (e.g., the PAM) in the principal component distributions, fermion spin configurations might be necessary to be fed into PCA directly. As noted above, the particular form of the HS transformation will likely be relevant to the answer. Complete resolution of this issue would be facilitated by a comparison of results for different forms of the HS transformation, for example, by using the rotation symmetric form introduced by Chen and Tremblay [54], but is beyond the scope of the present paper.

It remains to assess the extent of the advantages offered by machine learning approaches to these transitions. In the cases we have studied, traditional approaches based on analysis of the known order parameters would likely give a more accurate determination of the critical points. These more precise values are usually achieved only following a finite size scaling analysis, as discussed in the last paragraph of the Holstein model section. Finally, one should acknowledge that the more established methods have been improved and refined over three decades. Machine learning techniques for DQMC await a similar development and improvement process.

In particular, an intriguing opportunity is offered in cases where the sign problem makes the usual evaluation of a response function χ excessively noisy. Because the PCA does not involve the computation of the ratio $\langle \chi S\rangle/\langle S\rangle$, but rather only the generation and analysis of configurations of the Hubbard-Stratonovich field (with the absolute value of the determinants as the weight), it seems possible that insight into transitions beyond the sign problem might prove possible. One knows that if the sign is ignored, then the response functions can give incorrect information about the physics (in the case of the 2D repulsive Hubbard model a d-wave pairing amplitude that decreases as T is lowered instead of increasing) [67,74]. Understanding whether a machine learning analysis of the full space-time HS field configuration generated with the absolute value of the sign can provide greater insights into the properties of the model is an open question.

ACKNOWLEDGMENT

This work was supported by the Department of Energy under Grant No. DE-SC0014671 and by the Brazilian agencies Faperj and CNPq.

[1] J. Hopfield, Proc. Natl. Acad. Sci. USA **79**, 2554 (1982).
[2] D. J. Amit, H. Gutfreund, and H. Sompolinsky, Phys. Rev. A **32**, 1007 (1985).
[3] D. J. Amit, H. Gutfreund, and H. Sompolinsky, Phys. Rev. Lett. **55**, 1530 (1985).
[4] G. Toulouse, S. Dehaene, and J.-P. Changeux, Proc. Nat. Acad. Sci. USA **83**, 1695 (1986).
[5] N. Parga and M. Virasoro, J. Phys. France **47**, 1857 (1986).
[6] G. Parisi, J. Phys. A: Math. Gen. **19**, L675 (1986).
[7] M. Mézard, J. Nadal, and G. Toulouse, J. Phys. **47**, 1457 (1986).
[8] J. Liu, Y. Qi, Z. Y. Meng, and L. Fu, Phys. Rev. B **95**, 041101 (2017).
[9] L. Huang and L. Wang, Phys. Rev. B **95**, 035105 (2017).
[10] L. Wang, arXiv:1702.08586.
[11] L. Wang, Phys. Rev. B **94**, 195105 (2016).
[12] W. Hu, R. R. P. Singh, and R. T. Scalettar, Phys. Rev. E **95**, 062122 (2017).
[13] C. Wang and H. Zhai, Phys. Rev. B **96**, 144432 (2017).
[14] K. Ch'ng, J. Carrasquilla, R. G. Melko, and E. Khatami, Phys. Rev. X **7**, 031038 (2017).
[15] P. Broecker, J. Carrasquilla, R. G. Melko, and S. Trebst, Sci. Rep. **7**, 8823 (2017).
[16] E. LeDell, Prabhat, D. Y. Zubarev, B. Austin, and W. A. Lester, J. Math. Chem. **50**, 2043 (2012).
[17] X. Y. Xu, Y. Qi, J. Liu, L. Fu, and Z. Y. Meng, Phys. Rev. B **96**, 041119 (2017).

[18] J. Liu, H. Shen, Y. Qi, Z. Y. Meng, and L. Fu, Phys. Rev. B **95**, 241104 (2017).
[19] L. Huang, Y.-f. Yang, and L. Wang, Phys. Rev. E **95**, 031301 (2017).
[20] J. Carrasquilla and R. Melko, Nat. Phys. **13**, 431 (2017).
[21] G. Carleo and M. Troyer, Science **355**, 602 (2017).
[22] E. Van Nieuwenburg, Y.-H. Liu, and S. Huber, Nat. Phys. **13**, 435 (2017).
[23] Y. Zhang and E.-A. Kim, Phys. Rev. Lett. **118**, 216401 (2017).
[24] G. Torlai, G. Mazzola, J. Carrasquilla, M. Troyer, R. Melko, and G. Carleo, arXiv:1703.05334.
[25] Y. Zhang, R. G. Melko, and E.-A. Kim, arXiv:1705.01947.
[26] T. Ohtsuki and T. Ohtsuki, J. Phys. Soc. Jpn. **86**, 044708 (2017).
[27] F. Schindler, N. Regnault, and T. Neupert, Phys. Rev. B **95**, 245134 (2017).
[28] D.-L. Deng, X. Li, and S. Das Sarma, Phys. Rev. X **7**, 021021 (2017).
[29] L. M. Raff, M. Malshe, M. Hagan, D. I. Doughan, M. G. Rockley, and R. Komanduri, J. Chem. Phys. **122**, 084104 (2005).
[30] K. Ch'ng, N. Vazquez, and E. Khatami, arXiv:1708.03350.
[31] P. Broecker, F. F. Assaad, and S. Trebst, arXiv:1707.00663.
[32] T. Paiva, R. T. Scalettar, W. Zheng, R. R. P. Singh, and J. Oitmaa, Phys. Rev. B **72**, 085123 (2005).
[33] I. F. Herbut, Phys. Rev. Lett. **97**, 146401 (2006).
[34] F. F. Assaad and I. F. Herbut, Phys. Rev. X **3**, 031010 (2013).
[35] F. Parisen Toldin, M. Hohenadler, F. F. Assaad, and I. F. Herbut, Phys. Rev. B **91**, 165108 (2015).
[36] Y. Otsuka, S. Yunoki, and S. Sorella, Phys. Rev. X **6**, 011029 (2016).
[37] R. Blankenbecler, D. J. Scalapino, and R. L. Sugar, Phys. Rev. D **24**, 2278 (1981).
[38] J. E. Hirsch, Phys. Rev. B **28**, 4059 (1983).
[39] J. E. Hirsch, Phys. Rev. B **34**, 3216 (1986).
[40] K. Pearson, Philos. Mag. **2**, 559 (1901).
[41] Wikipedia contributors, Principal component analysis—Wikipedia, The Free Encyclopedia (2017).
[42] I. Jolliffe, *Principal Component Analysis Springer Series in Statistics* (Springer, New York, NY, 2002).
[43] P. Coleman, *Handbook of Magnetism and Advanced Magnetic Materials* (Wiley, New York, NY, 2007).
[44] S. Doniach, Physica B+C **91**, 231 (1977).
[45] C. Lacroix and M. Cyrot, Phys. Rev. B **20**, 1969 (1979).
[46] P. Fazekas and E. Müller-Hartmann, Z. Phys. B: Condens. Matter **85**, 285 (1991).
[47] F. F. Assaad, Phys. Rev. Lett. **83**, 796 (1999).
[48] N. C. Costa, J. P. Lima, and R. R. dos Santos, J. Magn. Magn. Mater. **423**, 74 (2017).
[49] M. Vekić, J. W. Cannon, D. J. Scalapino, R. T. Scalettar, and R. L. Sugar, Phys. Rev. Lett. **74**, 2367 (1995).
[50] C. Huscroft, A. K. McMahan, and R. T. Scalettar, Phys. Rev. Lett. **82**, 2342 (1999).
[51] T. Paiva, G. Esirgen, R. T. Scalettar, C. Huscroft, and A. K. McMahan, Phys. Rev. B **68**, 195111 (2003).
[52] W. Hu, R. T. Scalettar, E. W. Huang, and B. Moritz, Phys. Rev. B **95**, 235122 (2017).
[53] G. G. Batrouni and R. T. Scalettar, Phys. Rev. B **42**, 2282 (1990).
[54] L. Chen and A.-M. S. Tremblay, Int. J. Mod. Phys. B **06**, 547 (1992).
[55] D. Vollhardt, N. Blümer, K. Held, and M. Kollar, in *Band-ferromagnetism: Ground-state and Finite-Temperature Phenomena* (Springer, Berlin, Heidelberg, 2001), pp. 191–207.
[56] E. H. Lieb, Phys. Rev. Lett. **62**, 1201 (1989).
[57] S.-Q. Shen, Z.-M. Qiu, and G.-S. Tian, Phys. Rev. Lett. **72**, 1280 (1994).
[58] A. Mielke, J. Phys. A: Math. Gen. **24**, L73 (1991).
[59] H. Tasaki, Phys. Rev. Lett. **75**, 4678 (1995).
[60] H. Tasaki, Prog. Theor. Phys. **99**, 489 (1998).
[61] H. Tasaki, J. Phys.: Condens. Matter **10**, 4353 (1998).
[62] N. C. Costa, T. Mendes-Santos, T. Paiva, R. R. dos Santos, and R. T. Scalettar, Phys. Rev. B **94**, 155107 (2016).
[63] R. T. Scalettar, D. J. Scalapino, R. L. Sugar, and S. R. White, Phys. Rev. B **44**, 770 (1991).
[64] Z. B. Huang, H. Q. Lin, and J. E. Gubernatis, Phys. Rev. B **63**, 115112 (2001).
[65] Y. F. Kung, C.-C. Chen, Y. Wang, E. W. Huang, E. A. Nowadnick, B. Moritz, R. T. Scalettar, S. Johnston, and T. P. Devereaux, Phys. Rev. B **93**, 155166 (2016).
[66] R. R. dos Santos, Braz. J. Phys. **33**, 36 (2003).
[67] S. R. White, D. J. Scalapino, R. L. Sugar, N. E. Bickers, and R. T. Scalettar, Phys. Rev. B **39**, 839 (1989).
[68] R. T. Scalettar, E. Y. Loh, J. E. Gubernatis, A. Moreo, S. R. White, D. J. Scalapino, R. L. Sugar, and E. Dagotto, Phys. Rev. Lett. **62**, 1407 (1989).
[69] T. Paiva, R. R. dos Santos, R. T. Scalettar, and P. J. H. Denteneer, Phys. Rev. B **69**, 184501 (2004).
[70] T. Holstein, Ann. Phys. **8**, 325 (1959).
[71] M. Vekić, R. M. Noack, and S. R. White, Phys. Rev. B **46**, 271 (1992).
[72] R. M. Noack, D. J. Scalapino, and R. T. Scalettar, Phys. Rev. Lett. **66**, 778 (1991).
[73] N. C. Costa, W.-T. Chiu, and R. T. Scalettar (unpublished).
[74] E. Loh, J. Gubernatis, R. Scalettar, S. White, D. Scalapino, and R. Sugar, Intl. J. Mod. Phys. **16**, 1319 (2005).